ORIGINAL ARTICLE

lajss.org© Latin American Journal of Solids and Structures

www.lajss.org

CFRP repair effectiveness on compressed steel tubular members with circular cutout

Jorge Luis Martinez[a], Julio Cesar Ramalho Cyrino[a], Murilo Augusto Vaz[a]*, Irving David Hernández[a], Victor Daniel Torres[a], Valber Azevedo Perrut[b], Gustavo Gomes de Paula[b]

[a]Programa de Engenharia Oceânica, Universidade Federal do Rio de Janeiro, Rio de Janeiro, RJ, Brasil. E-mail: jlfernandez@oceanica.ufrj.br, julio@oceanica.ufrj.br, murilo@oceanica.ufrj.br, nxdavid@oceanica.ufrj.br, victordz@oceanica.ufrj.br

[b]PETROBRAS/CENPES, Rio de Janeiro, RJ, Brasil. E-mail: vperrut@petrobras.com.br, ggpaula@petrobras.com.br

*Corresponding author

https://doi.org/10.1590/1679-78257357

Abstract

Welding procedures for repairing corroded tubular structures are commonly used; however, composite material repairs are becoming popular since they do not use heat sources that might cause accidents. This paper provides a detailed description of the CFRP patch repair application in steel tubular members with a circular perforation originated from a prolonged corrosion process. The results of experimental tests on mid-scale unrepaired damaged and repaired steel tubes are reported. The predictions of the maximum loads recovered from a proposed numerical model lie close to the experimental observed values, justifying its usage for analysis of repaired tubular structures with circular cutouts when subjected to axial compression. Compared to unrepaired perforated tubes, the experimental results demonstrate a substantial strength recovery for repaired tubes. The value of this research for the oil and gas industry is that it demonstrates the feasibility of this kind of repair, which means reduced risk to the production unit and a shorter repair period.

Keywords

Corroded structures; Composite material repair; Steel tubular members.

Graphical Abstract

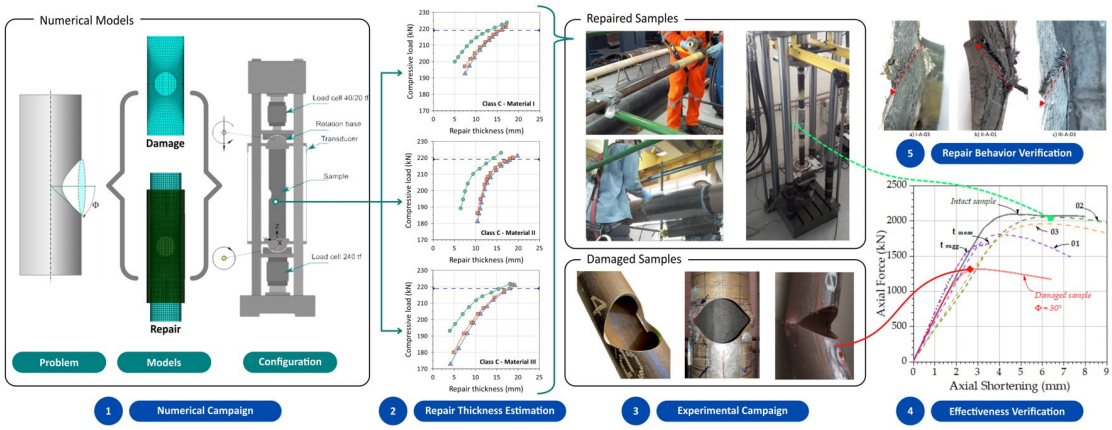

Received: October 28, 2022. In revised form: February 03, 2023. Accepted: February 06, 2023. Available online: February 07, 2023.
https://doi.org/10.1590/1679-78257357

1. INTRODUCTION

Offshore platforms that operate close to their lifespan limit commonly present structural deterioration associated with many types of damage, such as: impacts, corrosion, dents, cracks, and perforations. Each type of damage may affect the structure load bearing capacity in different ways; therefore, they require a particular analysis or investigation. The corrosion process in steel structures, for example, leads to the loss of material and, depending on its level, structural integrity can be severely compromised, creating conditions conducive to accidents or collapse of structures. The structural integrity assessment to determine the remaining strength of damaged structures often requires full-scale experimental results. However, this type of experimental campaign is usually expensive, thus numerical simulations can reduce the costs and facilitate the decision-making process when conducting a repair or replacement of the structure. The technical feasibility of this approach is based on the verification of the numerical predictions of a set of experimental tested mid-scale samples, allowing to delimit the deviation of the predictions with the response of real structures under controlled conditions.

There is a reduced number of works involved in evaluating damaged tubular members capacity, most of which focuses on impact dents (Cerik et al., 2016; Khedmati & Nazari, 2012; Yu & Amdahl, 2018; Zeinoddini et al., 2014), but do not assess the repair effectiveness. Pipe repair techniques based on composite materials have proven superior to other repair approaches because they are easy to apply and do not require welding or molds for injection of polymer material. Composite materials are easily adapted to geometric irregularities and studies to prolong the lifespan of damaged structures and pipelines are presented in the literature (Alexander & Bedoya, 2011; Alexander & Ochoa, 2010; Chan et al., 2015; Chen et al., 2016; Esmaeel et al., 2012; Mohammed et al., 2020; Siwowski & Siwowska, 2018; Subhani & Al-Ameri, 2016). Composite-based repairs have been performed on marine sand concrete pillars with fiber-reinforced polymers (FRP), which are widely used in coastal construction and marine infrastructure (Yang et al., 2020a, 2020b). Mohammed et al. (2020) and Vijay et al. (2016) employed FRP-based jackets as a form of repair for structures of steel-concrete. Tong et al. (2019) experimentally evaluated the use of carbon fiber reinforced polymer (CFRP) repairs to reduce the hot-spot stresses in tubular structures joints. Studies were also conducted to evaluate the remaining capacity of cylindrical steel structures with perforations derived from the presence of corroded regions without the correct protection. Okada et al. (2004) inferred the remaining strength of perforated tubular elements from formulations derived from previous experimental campaigns conducted by Nishimura et al. (1996) and Murakami et al. (1998). In these studies, the importance of perforation damage in the strength loss of tubular structures was addressed. It was possible to verify that depending on the axial location of the damage and its magnitude, if the tubular structure is sufficiently slender (intermediary to long columns), and subjected to a centralized axial compression load, this type of damage will promote the instability of the structure and eventual failure. However, if the structure is not sufficiently slender (short columns), it will fail due to a combination of initial crushing followed by elastoplastic instability. Vaz et al. (2018) presented a campaign of mid-scale experimental tests to determine the maximum strength of perforated steel tubes subjected to axial compression. Hernández et al. (2019) performed numerical simulations of the same samples considering initial imperfections due to machining or aging processes, through a three-dimensional prototyping and evaluated the error associated with the numerical predictions. Hernández et al. (2018) proposed a simplified expression to infer the remaining compressive capacity of perforated tubular members employing design-of-experiments (DoE) and genetic programming of evolutionary algorithms. In addition to this research, there are other studies available in the literature related to the structural integrity of steel dented tubes. There is scarce research on the topic of evaluating composite-based repairs for structural steel tubular members, and currently there are no recommendations in available standards for guidance on how to rationally specify the size (length and thickness) and application of composite-based repairs.

The flare-boom structure is a key component for the safe operation of oil and gas production platforms. This work addresses the CFRP-based repair of flare-boom steel tubular members, considering damage by perforation due to a state of chronic localized corrosion. The results of experimental investigations of perforated steel tubular structures (scale 1:3.5) subjected to axial compression and thermal loads are addressed. Samples were repaired with three distinct types of materials. The steel tubes' samples are representative of the longitudinal (L/R_g) and transversal (D/t) slenderness ranges of actual flare-boom tubular structures; where L, R_g, D and t denote, respectively, length, radius of gyration, outer diameter, and nominal thickness of the samples. A numerical modeling is employed for inferring the repair thickness dimensions.

2. MATERIALS AND METHODS

The current study is divided into two parts that describe the procedures, assumptions, and methodologies used to estimate the efficiency of CFRP-based repairs on compressed steel tube members with circular cutouts at half the length due to a chronological corrosion effect. The former section covers the numerical model and the protocol used to size a repair patch. The last section summarizes the experimental campaign as well as the lamination steps for each repair material.

2.1. Numerical model

The numerical models were created using the Python scripting interface of the ABAQUS (Dassault Systèmes, 2009) finite element (FE) software. The FE-element model was based on the assemble of two geometry parts through contact tie constrains, and double symmetry boundary conditions. Geometries of numerical models were created by shell surfaces as follows:

- **Tubular member:** Represented as a cylinder of diameter D, length L, and wall thickness t with one of its ends centered at the coordinates X = Y = Z = 0 and the other in X = Y = Z = L.
- **Perforation damage:** A cutout have been subtracted from the tubular member component in the modeling process. The cutout was created by first drawing a circular path with diameter $D_p = D \sin(\Phi)$ at the XZ-plane (center in Z = $L/2$), and then projecting that path upward until it intersected with the wall of the tubular part. After then, geometry was eliminated from the circular projection.
- **CFRP-patch repair:** A circular path of diameter $D+t_r$ (t_r is the repair thickness) is extruded symmetrically (over the Z-axis) from an XY-plane centrally positioned at Z = $L/2$ up to a distance equal to the effective overlap length (L_{eff}). The patch of repair is then created through the composite layup utility, with the extruded cylinder acting as the reference surface, and setting n-layers of composite material until meeting the required repair thickness (t_r).

2.1.1 Boundary conditions

Boundary conditions (BCs) are defined by considering the schemes in **Figure 1**. To reduce computational effort, edges S1, S2 (from tube geometry) and C1, C2 (from CFRP-patch) impose a symmetry constraint across the X-axis known as XSYMM (**Figure 1a**), while at edges S3, C3 a symmetry constraint is applied along the Z-axis, known as ZSYMM (**Figure 1b**). The X-axis translation (U1) and the Y and Z axes rotations (UR2, UR3) are constrained in the XSYMM constraint (U1 = UR2 = UR3 = 0). The Z-axis translation (U3) and the X and Y axes rotations (UR1, UR2) are constrained in the ZSYMM constraint as well (U3 = UR1 = UR2 = 0). The repair patch is then attached to the pipe using surface-to-surface tie constraints (B1), with the inner surface of the CFRP-patch repair acting as the slave entity and the outer surface of the tube acting as the master entity (**Figure 1c**). Finally, a rigid-link reference node (RP) to which the S2 contour was connected by TIE constraints was used to apply the loading condition considering U1 = U2 = UR2 = UR3 = 0, UR1 = Free, and U3 = δ_z (axial controlled displacement) as the RP's degrees of freedom (**Figure 1c**).

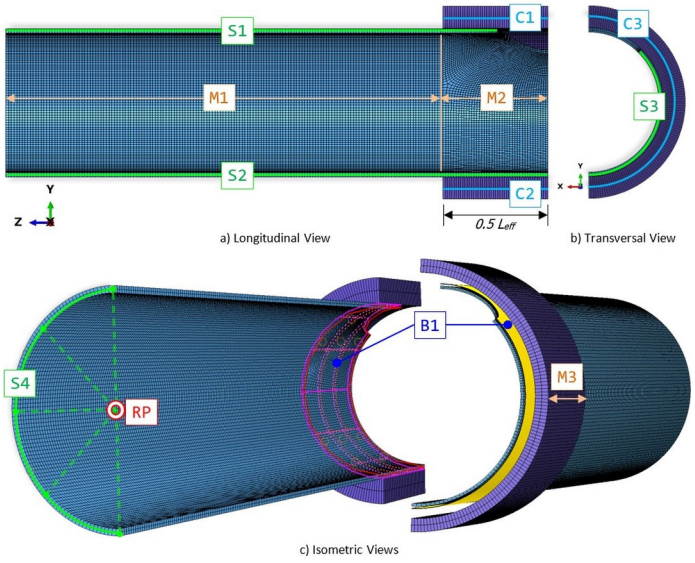

Figure 1: Numerical model mesh, boundary conditions and contact properties schemes.

From **Figure 1a,c**, the regions from tubular member M1, M2, and from CFRP-patch repair M3 can be used to characterize the mesh used for the numerical models. S4R element type, which is a 4-node double curved shell with reduced integration and hourglass control, is used for the meshes in all regions. The decision to use this type of element for modeling, instead of solid elements, was based on earlier research published in the literature (Kabir et al., 2016; Hassanein et al., 2017; Lan et al., 2017; Imran et al., 2018; Zhao et al., 2019; Liu et al., 2020; Tafsirojjaman et al., 2020; George et al., 2021). Conventional shell elements do not experience singularities at point or line loads, or sudden changes

of kinematic boundary conditions, in addition to requiring less computational effort than models based on solid elements. As the D/t ratios addressed in this study were between 15 and 35, and due to the nature of the loading scenario, this parameter has no significance on the model's compressive response justifying the use of shell elements, as reported by Vaz et al. (2018).

Structured element distribution with curvature refinement and $t/2$ maximum element size was used in regions M1 and M3. Region M2 employs a free-unstructured element distribution with a maximum element size of $t/6$, as well as a mesh transition optimization by the medial-axis algorithm. All regions used automatic element size reduction through curvature control and a proportion of global element size of up to 0.01t. The effective length of the CFRP repair is parametrically described as $L_{eff} = D_p + 2\ L_{ovp}$, where L_{ovp} is the overlap length with a constant value obtained using double lap-shear tests, according to ASTM D3528 (ASTM, 2016), as the greater value between $D/4$ and 200 mm, and D_p is the cutout diameter, which is a function of the perforation angle Φ, and specified as $D_p = D\ \sin(\Phi)$, with D being the tubular member's diameter.

2.1.2 Thermal effects

For simulating the thermal chamber heating, a sequential decoupled thermo-mechanical analysis was performed, initiating with a thermal analysis simulating the heating process followed by the compressive loading. The thermal load is imparted by the temperature distribution at the nodes from the outer surface of the repair to the inner surface of the steel tube inside the thermal chamber length, according to the values provided by the thermocouples installed in the samples. Temperatures vary over time, from ambient temperature to operating temperature T_m, for each type of material (I, II and III). With the temperature field, at the nodes of the mesh of the interface and composite laminate, a thermomechanical analysis is performed to determine the deformations during the temperature rise process. Thermal properties such as conductivity ($k_{1(hoop)}$, $k_{2(axial)}$) and coefficient of thermal expansion ($\alpha_{1(hoop)}$, $\alpha_{2(axial)}$), for the repair material type I, were respectively $k_{1(hoop)}$ = 0.6 E-3 W/(mm °C), $k_{2(axial)}$ = 3.9 E-3 W/(mm °C), $\alpha_{1(hoop)}$ = 5.8 E-6 °C^{-1}, and $\alpha_{2(axial)}$ = 18.5 E-6 °C^{-1}, retrieved from the material datasheet. For repair material types II and III, the values were obtained from Joven and Minaie (2018) as: $k_{1(hoop)} = k_{2(axial)}$ = 0.573 E-3 W/(mm °C), and $\alpha_{1(hoop)} = \alpha_{2(axial)}$ = 21.0 E-6 °C^{-1}.

The mechanical properties of steel were assumed to be constant with temperature, given the relatively small operating temperatures.-The maximum working temperature (T_m) for the repair was determined experimentally, in accordance with ISO/TS 24817 (ISO, 2006), assuming that $T_m = T_g - 30$ °C (where T_g is the glass transition temperature), to prevent softening of the resin and laminate. The glass transition temperatures for composite materials and resins were established by DMA experiments according to ASTM D5023 (ASTM, 2015), where T_g was taken to be the peak of a tan(δ)-to-temperature curve. **Table 1** summarizes the glass transition temperature values for resin ($T_{g.r}$) and composite material ($T_{g.c}$). It should be noted that due to rapid deterioration within the glass transition zone, Material II reached lower temperatures than Materials I and III for both the composite material and the resin.

Table 1: Summary of temperatures by repair material type.

	COMPOSITE PATCH REPAIR		
TEMPERATURE	**MATERIAL I**	**MATERIAL II**	**MATERIAL III**
Operating temperature – T_m	127 °C	90 °C	140 °C
Resin glass transition temperature** – $T_{g.r}$	168 °C	108 °C	162 °C
Composite material glass transition temperature** – $T_{g.c}$	157 °C	119 °C	172 °C

** Average value recovered from at least three specimens.

2.2. Experimental campaign

To verify the performance of CFRP-based repairs, a series of experiments were carried out using three different repair materials. Mid-scale samples with representative values of flare-boom steel tubular structures, $L/r_g \in \{10, 45\}$ and $D/t \in \{15, 35\}$, were submitted to axial compression by means of controlled displacement. In addition, thermal loads were applied to the samples using a customized thermal chamber to infer the thermal effects on the performance of the composite repairs.

2.2.1. Experimental setup

A series of axial compression tests on tubular steel structures intact, damaged by perforations, and CFRP-repaired were carried out in the Ocean Structures Nucleus laboratory (NEO/COPPE) of the Federal University of Rio de Janeiro. The tests were performed on a universal testing machine MTS 311.41 with a capacity of 2.5 MN, following the configuration illustrated in **Figure 2**. This arrangement mimics a simply supported column beam, ensuring a scenario of pure axial compression. The

load was imposed through controlled vertical displacement using the apparatus internal sensor (LVDT) and the reaction load was measured with a load cell located at the bottom of the samples. Data acquisition from all sensors was performed using a NI-cDAQ 9188 system, with C modules for different types of signals, using the LabVIEW platform.

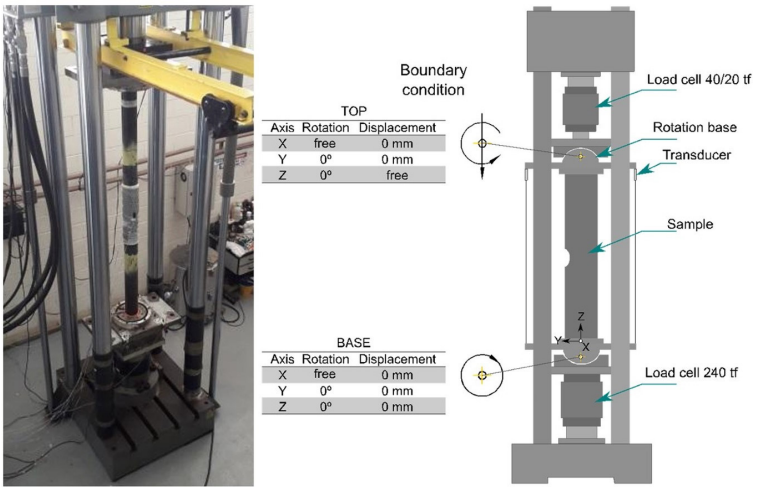

Figure 2: Experimental setup and boundary conditions of the tests.

To carry out the tests at operating temperature of common flare-boom structures, a cylindrical bipartite thermal chamber was designed and built (see **Figure 3a**). This chamber is open for sample placement in the center after being installed in the test equipment. Two sets of bisected plates were used to adjust the chamber to the sample diameter, to avoid the hot air to escape through the openings. Internal heating was achieved by a 440v electrical resistance coil fixed to the chamber inner wall and an air injection system was designed to force circulation and improve temperature equalization inside the chamber. **Figure 3b** shows an internal view of the thermal chamber, where it is possible to identify the opening for the tubular repair elements entry at the bottom, and the resistance coil fixed to the walls. The temperature monitoring was performed by using five K-type thermocouples Model TFCY-015-50, which were fixed on the inner and outer surfaces of the laminate.

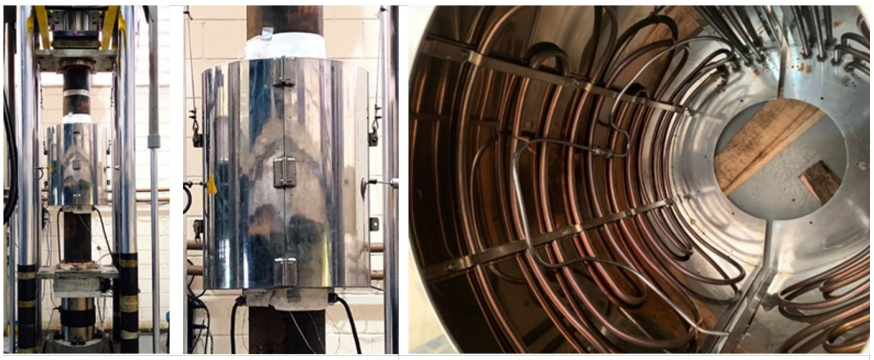

a) Thermal chamber external view b) Thermal chamber inner view

Figure 3: Customized bipartite thermal chamber for samples heat application.

2.2.2. Experimental samples

The dimensions of experimental samples are in a 1:3.5 scale retrieved from real flare-boom structures. In this study, it was assumed an extended deterioration of the external wall, due to severe localized corrosion, represented by a circular cutout located at the half-length of the samples. **Figure 4a** is an example of a damaged steel tubular member sample, and **Figure 4b** presents a scheme of the angle of damage Φ that parameterizes the cutout path.

Tubular structures of API 5L grade B steel was used for test samples fabrication, and classified by its geometrical characteristics in classes A, B and C arbitrarily. **Table 2** presents the main properties by class type of the tubular member samples employed in the experiments.

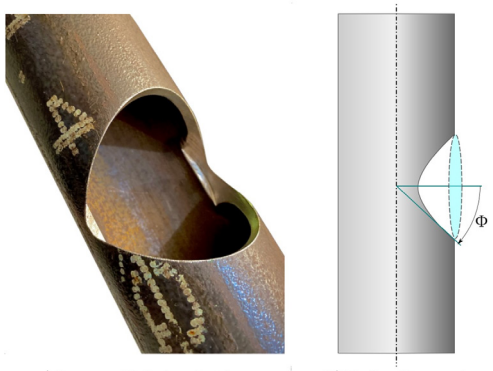

Figure 4: Damaged steel tubular structures schemes.

Table 2: Properties by class type of tubular member samples.

	TUBE CLASS		
PROPERTY	**A**	**B**	**C**
Length - *L* (mm)	2000	2100	2400
Outer diameter - *D* (mm)	273.0	114.3	60.3
Nominal thickness - *t* (mm)	7.83	6.35	3.91
Damage angle - Φ (deg)	30	60	90
Cutout diameter - D_p (mm)	136	100	60
Yield stress - σ_y (MPa)	321	350	390
Young's modulus - *E* (GPa)	200	200	205
Poisson's coefficient - *v*	0.3	0.3	0.3
Ultimate tensile stress - σ_u (MPa)	557	605	612
Maximum elongation - ε_u (%)	17.7	19.4	16.3

2.2.3 Composite repair materials

Three different composite materials of plain carbon fiber and carbon fiber mixed with fiberglass are considered for the patch repair. Each repair material option is identifiable by a roman number: **Material I** is a plain carbon glass/epoxy hybrid composite laminate impregnated with epoxy resin, with 0°/90° fiber orientation and 0.457 mm (200 g/m^2) ply thickness. In 0° the carbon fibers are longitudinally aligned; in 90° direction glass fibers provide circumferential stiffness and strength. Minimum time from lamination to its use is 240 h for curing at room temperature with 100:27 resin-catalyst mixture ratio per weight. **Material II** is a composite carbon/epoxy single-ply laminate (CFRP), with 0°/90° orientation of 12k-type carbon fiber and 0.400 mm (302 g/m^2) ply thickness, impregnated with Epoxy resin. The curing occurs at room temperature, using the matrix formulation Butanox M-50 catalyst and Cobalt/NafCo initiator. **Material III** is a composite carbon/epoxy single-ply laminate (CFRP), with 0°/90° orientation and 0.196 mm (200 g/m^2) ply thickness. The matrix is composed of Araldite-GY-260 resin and XB-3473 hardener. The resin-hardener blend ratio, as per the manufacturer's guidance, is 100:23 per weight. The resin cure is performed using a thermal blanket. The fabric with an orientation of 0/90 in regard to the longitudinal direction of the tube was chosen for two reasons: first, to facilitate lamination, and second, to place fibers in the direction of the load (0°) while strengthening the tube in the cutout region in the transversal direction.

2.3 Repair thickness

For the patch repair, tensile, compression, and shear tests were conducted to determine the mechanical characteristics of repair materials, and the results, which were employed in numerical models to determine the repair thickness, are summarized in **Table 3**.

Table 3: Composite material's mechanical properties.

CFRP-PATCH	E_1 (GPa)	E_2 (GPa)	ν_{12}	G_{12} (GPa)	G_{13} (GPa)	G_{23} (GPa)
Material I	38.20	6.50	0.44	4.70	4.21	4.21
Material II	31.60	31.60	0.19	1.73	1.73	1.73
Material III	31.94	31.94	0.26	2.93	2.93	2.93

Numerical simulations were conducted to determine the maximum compressive capacity for steel tubular members with different repair thicknesses, repair Materials I, II, and III, and cutout damages Φ = {30°, 60°, 90°}. The simulations were carried out by raising the repair thickness until the maximum strength of an undamaged (intact) steel tube was established. **Table 4** depicts the maximum loads obtained by the numerical model for intact and unrepaired damaged steel tubular members of Class A, B, and C members. It is evident that the tube's slenderness and cutout size have a negative impact on compressive capacity. It should be noted that due to the large cylindrical hinge dimensions (and inertia) of the experimental interfaces, and the slender level of class C tubes, a change in boundary conditions was detected which resulted in imposing a quasi-fixed support on the sample lower end during loading, preventing the free hinge rotation. Thus, the models to retrieve repair thickness for samples from class C imposed a rotation restriction at the bottom end, assuming fixed boundary conditions.

Table 4: Maximum compressive loads of unrepaired damaged steel tubes.

Angle Φ (deg)	Class A (kN)	Class B (kN)	Class C (kN)
Intact	2100	670	219
30°	1350	409	169
60°	627	180	74
90°	454	135	40

The thickness values proposed for repairing the experimental samples are summarized in **Table 5**. These thicknesses were determined from the maximum compressive load curves as a function of repair thickness, at the points where the curves intersected the intact load lines (see **Figure 5**).

Table 5: Summary of thicknesses for experimental samples repair.

Composite Type	Class A (Φ = 30°) Repair thickness (mm) Suggested / Required	Class B (Φ = 60°) Repair thickness (mm) Suggested / Required	Class C (Φ = 90°) Repair thickness (mm) Suggested / Required
I	10.1 / 12.8	13.7 / 12.3	6.9 / 5.9
II	8.0 / 22.8	10.0 / 22.8	10.0 / 9.2
III	8.0 / 7.1	8.0 / 10.0	5.9 / 5.5

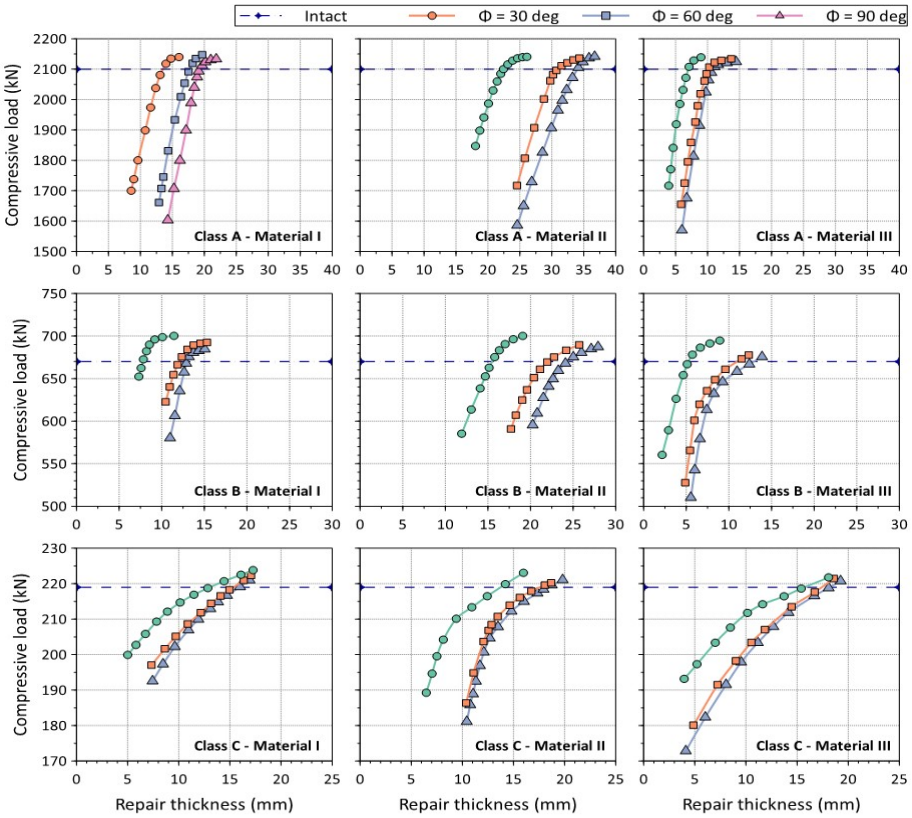

Figure 5: Compressive response as a function of the repair thickness.

For each type of repair material (I, II and III) nine repairs were performed on tubular samples of three different classes (A, B and C), using different repair procedures for each type of material. Three repaired samples were tested at maximum operating temperature. The compressive load bearing capacity of the repaired tubular members was then compared with its corresponding performance for intact tubes, whose experimental tests and numerical studies were addressed by Vaz et al. (2018).

2.4 Repair protocol

The protocol adopted to repair samples of tubular steel structures with circular cutouts using three different laminated composite materials is here described. A total of nine samples for each type of repair material, with circular cutouts at half of their length (*L/2*) were repaired for tubes Class A, B and C (see **Figure 6**). To prevent galvanic corrosion between the CFRP repair and the steel tube, a first layer of fiberglass was applied to the surface of the tube serving as an corrosion barrier (Hollaway & Cadei, 2002). The repair protocol for each composite material is briefly described in following paragraphs.

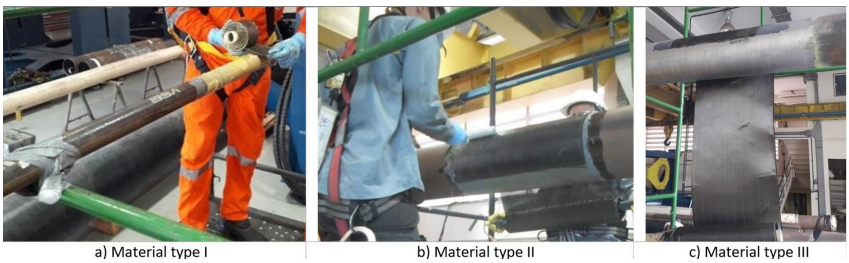

a) Material type I b) Material type II c) Material type III

Figure 6: CFRP-based repair being applied to different samples.

For **Material I**, the steel surface was initially prepared through mechanical grinding followed by blasting with a pneumatic rotating brush on the sanded area. Then, the surface roughness was measured at different points on the sanded surface, and a digital meter was used to obtain the profiles and average values of roughness. To avoid the formation of a protrusion during the lamination of the composite material over the cutout, thin steel sleeves were shaped to cover the void and provide continuity to the external surface of the tube. This cutout's cover does not play any structural role, so it is possible to manufacture it with any sufficiently rigid and thin material, if it can be molded to perform its supporting function. To avoid galvanic effects, fiberglass was used as the first layer between the steel substrate and the carbon layer. Then, manual layup process was used, impregnating the Type I material fabric with epoxy resin. **Figure 6a** shows the winding of Type I fabric on the surface of the Class C tube in the repair region.

For **Material II**, the surface was initially polished using a rotating brush. Then, surface roughness measurements were performed using a portable roughness meter. The roughness depth value (RT) was used as a parameter of measurement, and values greater than RT = 40 μm are considered acceptable. To enable the lamination over the cutouts, lids of galvanized steel with a thickness of 0.4 mm were molded. Before the layup process, a primer is applied to the tube surface in the repair region, and a layer of polyamide fabric 0.13 mm thick (PEEL-PLY) is manually rolled over it. After 12 hours for the primer cure under ambient conditions, the PEEL PLY is removed producing a surface with good roughness quality for the lamination. The first repair ply consists of fiberglass and then the carbon fiber layers are laminated. In the manual layup process, with the help of a roller, the fiber is impregnated with an epoxy resin and the fiber fabric positioned on the tube surface (**Figure 6b**).

For **Material III**, surface preparation was carried out using a pneumatic descaling machine. For each tubular element the perforation was covered with prefabricated carbon fiber composite sleeves with curvatures equal to the tube surfaces. Then, the carbon fiber fabric is manually rolled up on the tube surface and at the same time it is impregnated with the polymeric matrix. After the lamination procedure, a fiberglass tape is placed to promote a compaction of the laminate. Also, a perforated plastic over the laminate's compaction layer was placed and three "J" type thermocouples were attached to temperature control. For the resin curing process an electric thermal blanket (2880 W/220 v) was placed on the reinforced plastic cover in the repair region. The thermocouples and control of the electrical resistances of the thermal blanket were connected to an equipment specified as "hot bonder", which may be used to control localized heat sources for a wide variety of manufacturing and repair applications. Finally, after cooling the heated parts, the thermal blanket and the perforated plastic cover are removed, leaving the exposed repair. **Figure 6c** shows a manual impregnation of Class A tube.

3. RESULTS AND DISCUSSION

3.1. Ultimate strength

Global behavior was studied by comparing, numerically and experimentally, the axial compressive load and the longitudinal shortening responses at operating (T_m) temperatures. Additionally, the curves of experimental tests at room

temperature for intact and unrepaired tubes obtained in (Vaz et al., 2018) are presented, except for the 4" nominal diameter samples, where the experimental results are replaced by numerical simulations. These results quantitatively show the capacity recovery of repaired samples.

The adopted nomenclature for sample identification is: Material type (I, II and III), Tube class (A, B and C) and sample specification (01, 02 and 03), this latter represents the tubes tested at operating temperature for each type of material. It can also be seen the results of the numerical simulations with the suggested repair thickness of the composite laminate as *t*sugg, and with the average thickness of the repairs measured in the samples as *t*meas. **Figure 7** shows the Force-Displacement curves for numerical and experimental samples repaired with material type I. The maximum compression capacity, from numerical predictions and experimental measurements, of the samples of Class A, B and C reported close values with differences within the range of -4% to 1%, 4% to 14%, and -20% to 1%, respectively. The smaller capacity reported in sample Class C-02 (-20%) was due to the repair thickness being smaller than suggested. In general, repaired samples reported a recovery of the compressive capacity of ~96% of the intact condition, except for the tube Class C-02, suggesting a good performance of the laminate repairs. The effect of the operating temperature resulted in a reduction of the axial elastic stiffness in all samples, as well as a small influence on the maximum capacity load, decreasing approximately 8% in relation to the repaired tubes, except for the Class C-02 sample.

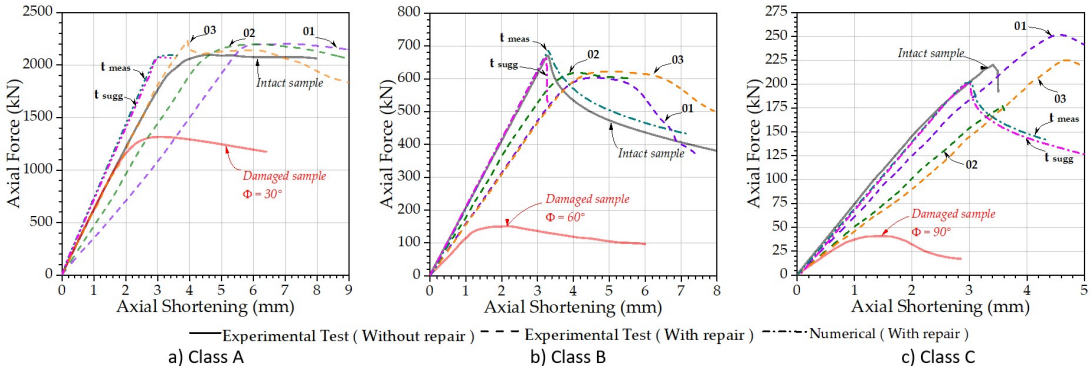

Figure 7: Load-shortening curves of samples repaired with material I.

Figure 8 shows the repaired samples' final states after compression at the operating temperature T_m = 127 °C. **Figure 8a** evidences a fracture on the laminate, in the half length of sample Class A-01, close to the cutout damage region in the post-buckling state. **Figure 8b,c** shows the repaired samples Class B-02 and Class C-01, without any apparent laminate failure, suggesting a buckling failure at a region outside the repair.

Figure 8: Damaged steel tubular structures repaired with material I.

Figure 9 presents the load-shortening curves for samples repaired with material II. Experimental responses of Class A samples reported close maximum responses, except for the sample Class A-01 that registered a maximum capacity ~15% smaller than those of the intact sample. In samples from Class B, the capacity recovery was in the order of ~80% of the intact sample. The numerical predictions were also lower than the intact tube, this was due to the repair thickness being smaller than necessary and the low compressive stress level of the repair material II. The experimental results of samples from class C reported a full recovery of the intact compressive capacity, except for sample Class A-01 being 11% lower than those of the intact sample. In contrast, comparing the experimental results and the numerical predictions, both had similar values, suggesting the numerical modeling prediction's reliability.

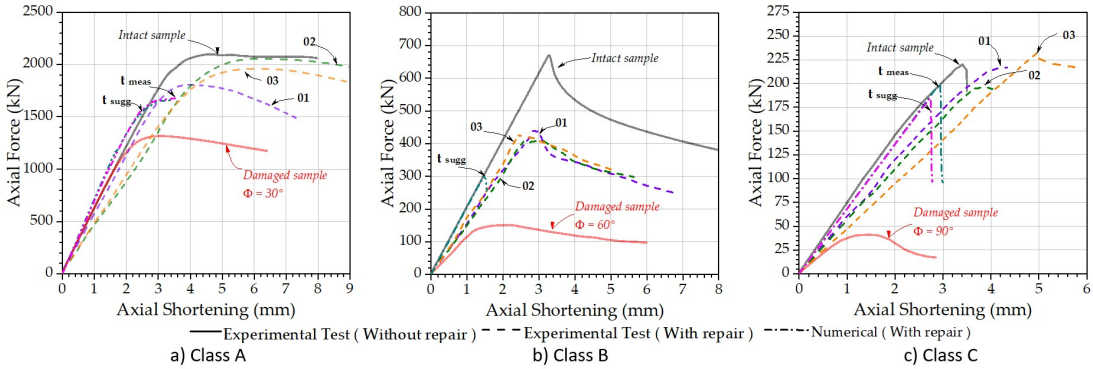

Figure 9: Load-shortening curves of samples repaired with material II.

Figure 10 shows results after buckling for Class A-01, Class B-03 and Class C-03 samples. Class A samples reported a plastic behavior followed by a carbon fiber rupture in the cutout neighborhood, as shown in **Figure 10a**. Classes B and C samples do not show composite laminate evident failure, being characterized by a failure based on elastoplastic and elastic buckling respectively (see **Figure 10b,c**) of the steel tubular member.

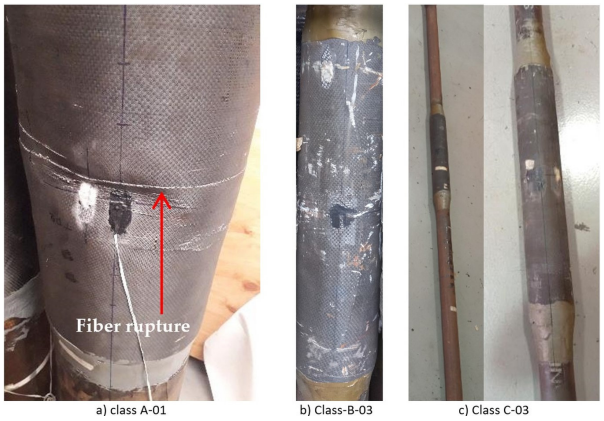

Figure 10: Repaired samples after being tested with material II.

Figure 11 shows the load-shortening curves for samples repaired with material type III. The experimental results for Class A samples were in the range of 14% to 15% lower than the intact sample (see **Figure 11a**). Samples A-01, A-02 and A-03 had stiffness close, larger and lower than that of the intact sample, respectively. The numerical predictions *t*sugg and *t*meas capacity values were ~1% greater than for the intact sample, as well as presenting slightly higher stiffness.

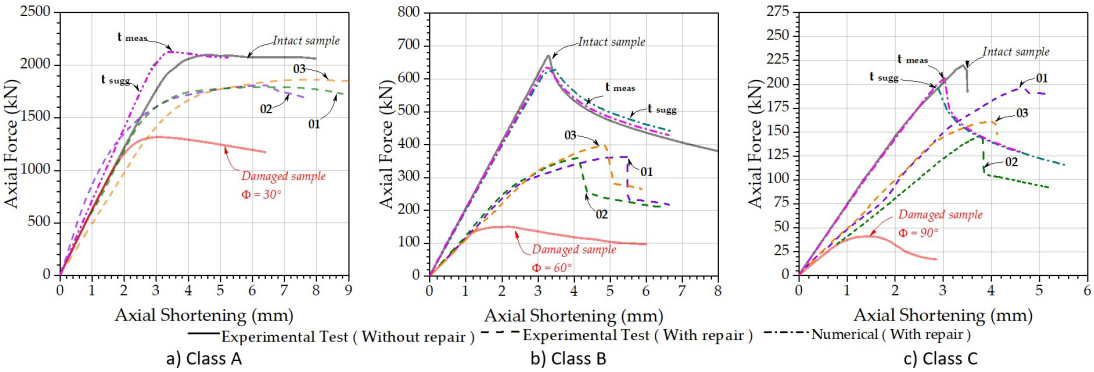

Figure 11: Load-shortening curves of samples repaired with material III.

The results of Class B samples evidenced lower performance when compared to intact samples. Samples B-01 and B-02 showed capacity values ~54% lower than those of the intact sample, and sample B–03 capacity was ~60% smaller (see **Figure 11b**). These samples also have much lower linear elastic stiffness than the intact tube (numerically and experimentally). These results could be related to problems encountered during the lamination process. Despite the lower performance, the load capacity recovery was ~107% relative to the unrepaired damaged samples. From **Figure 11c**

it can be observed that the repaired samples from Class C had lower stiffness level than the intact sample. Numerical predictions report capacity loads close to the intact experimental sample, and a slightly lower elastic stiffness. As the samples tested at operating temperature had capacity recovery in the order of ~76% of the intact sample, it can be said that the repair performances were also below expectations.

Figure 12 shows the status of repaired samples after execution of A-03, B-01 and C-01 samples tests. It can be observed that samples of Classes A and B experienced laminate failure in the damaged region as shown in **Figure 12a,b**. This failure may be associated with increased bending in the damaged region, promoting an increase in stress concentration. No laminate failure was evident in the Class B samples repaired with materials I and II, but buckling failure was recorded in the unrepaired region. Likewise, Class C samples do not show laminate failure, but do show buckling in the unrepaired regions for all repair materials (**Figure 12c**).

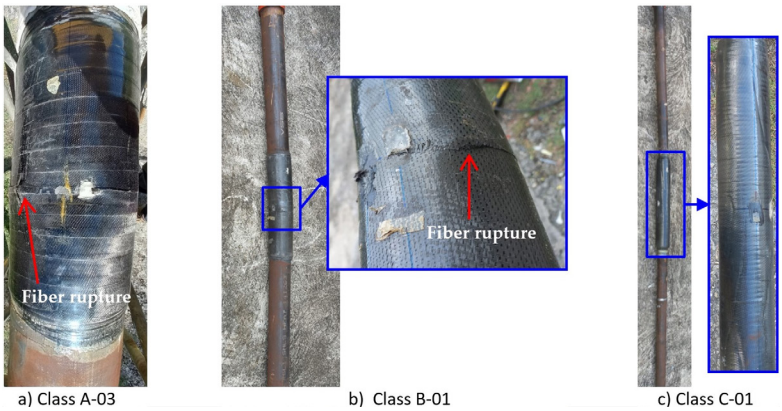

Figure 12: Repaired samples after being tested with material III.

3.2. Comparison of the maximum responses

The value of the maximum loads from experimental tests are relevant to assess the repair performance. **Table 6**, **Table 7**, and **Table 8** summarize, respectively, the values of samples from classes A, B and C for the measured repaired thicknesses (t_r), maximum loads (F_{max}) from experimental tests and numerical predictions, as well as the maximum load ratios. These ratios are given in percentage in the three last columns of the tables and correspond to the degree of the repair efficiency in relation to the intact sample ($\Delta F_1/F_{int}$) and to the sample with perforation ($\Delta F_2/F_{cutout}$), and the capacity difference of the numerical prediction relative to the experimental response ($\Delta F_3/F_{max}$). Where $\Delta F_1 = F_{max} - F_{int}$, $\Delta F_2 = F_{max} - F_{cutout}$, and $\Delta F_3 = F_{num} - F_{max}$, considering that F_{int}, F_{cutout} and F_{num} respectively denote the maximum loads of the intact, perforated, and numerical simulation samples. The numerical simulations were performed with repair thicknesses determined in the preliminary analyzes (suggested thicknesses) and with the average thicknesses of the repairs measured in the experimental samples, respectively denoted *t*sugg and *t*meas. In each table all these results are shown for each type of material used in the repairs. From **Table 6** for Class A repaired samples, the maximum loads for type I material exceed the intact tube load between 4% and 7%, and the perforated tube between 62% and 66%. The numerical predictions for the repaired tube proved a good correlation with differences between -4% and -6% of the experimental values. For repairs performed with type II material, the maximum loads were between -15% and -5% of the intact tube load, and the perforated tube between 33% and 53%. It can also be seen that the numerical prediction of the maximum load was between -8% and -20%. On the other hand, the performance with type III material presented the lower maximum loads around 15% of the intact tube load and 31% and 34% for perforated tubes. The numerical prediction overestimates between 17% and 20% the maximum load of the repaired tube.

From **Table 7** for Class B repaired samples, the patch repair of Type I material presented lower maximum loads than those of the intact tube, between 7% and 10%, although an increase in maximum load relative to perforated tube lays between 236% and 244%. As can be seen, the numerical prediction overestimated between 11% and 14%. For type II repairs, the maximum loads were below that of the intact tube, with differences between 34% and 39% and perforated tube between 128% and 144%. The numerical prediction of the maximum load underestimates its value by 26% and 31%. For the repairs performed in samples III-B-01, 02, 03, the maximum loads were far below the intact tube load, around 46%, and the repaired tube was close to 100%. The numerical prediction of the maximum load overestimates within the range of 71% to 89%.

Table 6: Measured maximum forces from numerical and experimental samples for Class A.

Material Type	Sample	t_r (mm)	F_{max} (kN)	$\Delta F_1/F_{int}$ (%)	$\Delta F_2/F_{cutout}$ (%)	$\Delta F_3/F_{max}$ (%)
	01	13.8	2190	4	62	-4
	02	13.8	2190	4	62	-4
I	03	14.0	2240	7	66	-6
	tsugg	10.1	2073	-1	54	1
	tmeas	13.6	2100	0	56	-
	01	8.9	1790	-15	33	-8
	02	9.3	2060	-2	53	-20
II	03	9.1	1990	-5	47	-17
	tsugg	8.0	1650	-21	22	-
	tmeas	9.0	1654	-21	23	-
	01	6.7	1780	-15	32	19
	02	7.0	1775	-15	31	20
III	03	6.6	1810	-14	34	17
	tsugg	8.0	2129	1	58	-
	tmeas	7.1	2122	1	57	-

Table 7: Measured maximum forces from numerical and experimental samples for Class B.

Material Type	Sample	t_r (mm)	F_{max} (kN)	$\Delta F_1/F_{int}$ (%)	$\Delta F_2/F_{cutout}$ (%)	$\Delta F_3/F_{max}$ (%)
	01	17.2	605	-10	236	14
	02	16.9	620	-7	244	11
I	03	16.9	620	-7	244	11
	tsugg	13.7	664	-1	269	4
	tmeas	17.3	689	3	283	-
	01	9.8	440	-34	144	-31
	02	10.1	410	-39	128	-26
II	03	10.2	430	-36	139	-29
	tsugg	10.0	304	-55	69	-
	tmeas	10.0	304	-55	69	-
	01	10.4	360	-46	100	89
	02	8.0	360	-46	100	89
III	03	8.9	400	-40	122	71
	tsugg	8.0	680	1	278	-
	tmeas	9.1	682	2	279	-

Table 8: Measured maximum forces from numerical and experimental samples for Class C.

CFRP-PATCH	SAMPLE	t_r (mm)	F_{max} (kN)	$\Delta F_1/F_{int}$ (%)	$\Delta F_2/F_{cutout}$ (%)	$\Delta F_3/F_{max}$ (%)
	01	15.3	252	15	530	-20
	02	9.8	180	-18	250	12
Material I	**03**	10.7	225	3	360	-10
	tsugg	13.7	200	-9	400	1
	tmeas	15.3	202	-8	405	--
	01	11.7	218	0	450	-9
	02	11.5	195	-11	390	2
Material II	**03**	11.8	232	6	480	-15
	tsugg	13.2	202	-70	12	-2
	tmeas	11.7	198	-70	10	-
	01	13.2	193	-12	380	7
	02	12.8	146	-33	270	40
Material III	**03**	13.0	162	-26	310	28
	tsugg	12.0	200	-70	11	4
	tmeas	13.0	207	-69	15	-

From **Table 8** for Class C samples, repaired samples of type I material exceeded the intact maximum capacity in the range of 3% to 15%, and a case with an 18% lower value, because the repair thickness was lower than the suggested thickness. The maximum load of the perforated tube lies between 250% and 530% higher. The numerical prediction underestimates the maximum load in two tubes by 20% and 10%, and in another one the load is overestimated by 12%. For type II repairs, the maximum loads were very close to the intact tube load, that is, between -11% and 6%. The maximum load increase of the perforated tube is between 390% and 480%. It can also be seen that the numerical prediction of maximum load showed strength improvements, with differences less than 15%. For repairs performed with type III material, the maximum loads were below the intact tube between 12% and 33%, and perforated tube between 270% and 380%. The numerical prediction overestimates the maximum load in the range of 7% to 40%.

Figure 13 shows a comparison for the maximum compressive load of experiments (01, 02 and 03) and numerical simulations (*t*sugg -suggested thicknesses; *t*meas - measured repairs average thicknesses), for each sample Class (A, B and C) and repair material (I, II and III). Almost all numerical predictions reported load responses close to the experimental measurements. The only exception was Class B specimens repaired with Type III material, which may be an effect associated with problems during the repair lamination phase.

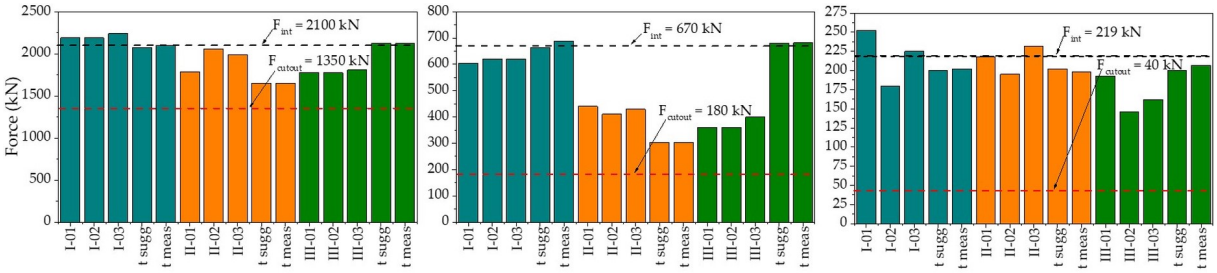

a) Class A (Φ = 30 deg) b) Class B (Φ = 60 deg) c) Class C (Φ = 90 deg)

Figure 13: Maximum Force of repaired samples.

3.3. Localized buckling

Vaz et al. (2018) evaluated tests of unrepaired perforated tubes, where localized buckling was observed with the development of almost symmetrical folding at the sides of the perforation (see **Figure 14**), an increment in the ovalization and a plasticization that propagates to adjacent regions.

a) Class A (Φ = 30 deg) b) Class B (Φ = 60 deg) c) Class C (Φ = 90 deg)

Figure 14: Localized buckling at samples without repair.

To observe the localized buckling in the repair region, it was necessary to dissect the laminate to expose the steel region around the damage. This was carried out for a sample of each class, for each repair material. **Figure 15a-c** shows a comparison of failures in the damaged region (post-buckling) for Class A samples, for each repair material. Sample I-A-03 (**Figure 15a**) shows a lower degree of folding on the sides of the cutout than a sample of the same damage without repair (**Figure 14a**), suggesting that the laminate prevented ovalization in the damaged region, thus increasing the compressive capacity. In this repaired sample, there was a load increase of ~140 kN compared to the intact sample. This is likely due to the 14 mm repair thickness (greater than the suggested 10 mm). **Figure 15b** shows the cutout shape of sample II-A-01 where an asymmetrical shape is observed on the sides of the cutout, suggesting a local effect of the laminate by locally increasing the stiffness, containing the hoop displacements. This sample suffered a load reduction of ~310 kN compared to the intact sample. From the post-buckling result of tube III-A-03 shown in **Figure 15c**, a lower level of fold similar to tube I-A-03 was observed. This sample also experienced a load reduction of ~290 kN compared to the intact sample.

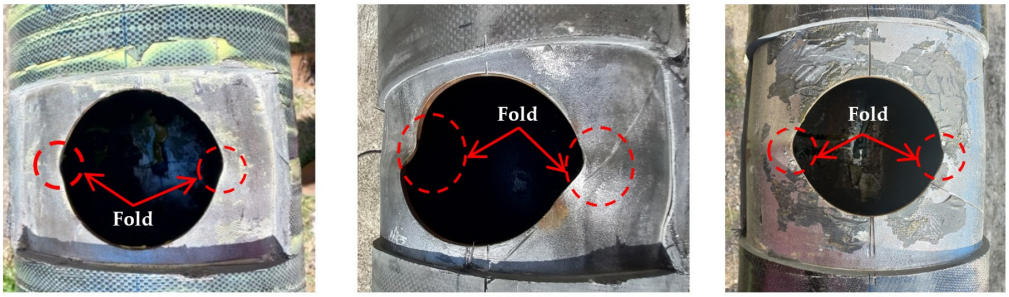

a) I-A-03 b) II-A-01 c) III-A-03

Figure 15: Localized buckling in samples of tubes from class A.

Similar to class A samples, the composite laminate was dissected in the damaged region of tubes B and C for each type of repair material (see **Figure 16**). The comparison of failure modes of samples I-B-03, II-B-03 and III-B-01 is presented respectively in **Figure 16a-c**. In the repair with type I material, no folds were identified on the sides of the perforation, nor significant ovalization. In repairs with materials II or III, a small level of fold was identified on the sides of the perforation, as well as lower recovery of the compressive load (**Figure 16b,c**). Likewise, the failure modes of samples I-C-03, II-C-03 and III-C-01 are shown respectively in **Figure 16d-f**. In these tubes class, the post-failure is characterized by folds close to the perforation without repair. In all the images it is observed that the folds do not appear, which means that the repair prevented the development of this failure mode.

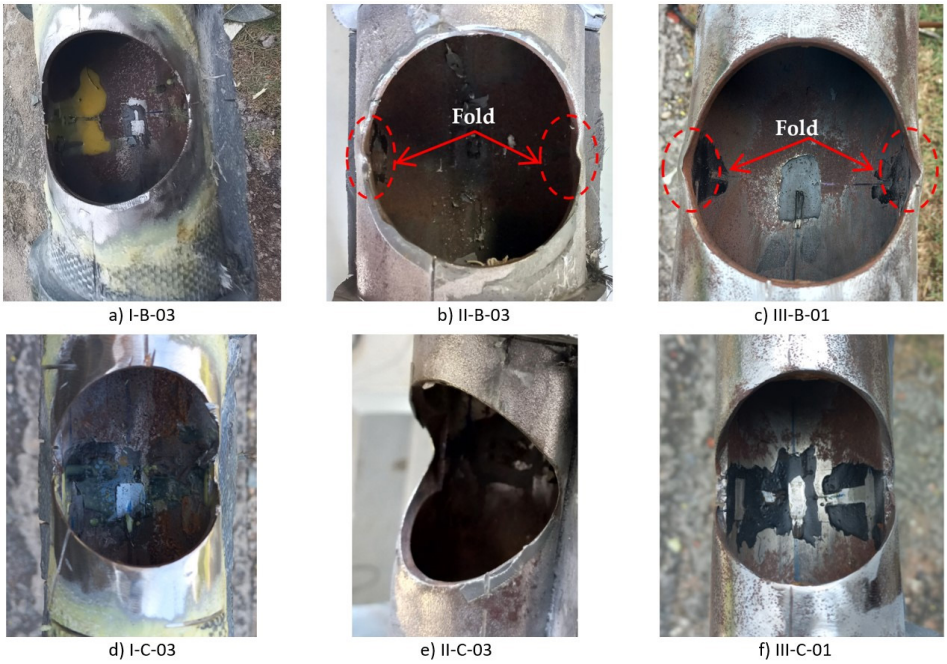

a) I-B-03 b) II-B-03 c) III-B-01

d) I-C-03 e) II-C-03 f) III-C-01

Figure 16: Localized buckling for samples of tubes from classes B and C.

3.4. Failure Mode

The failure mechanism of the samples was characterized by visual inspection, through longitudinal and transverse dissections of Class A, B and C samples. Note that the analysis of the sample conditions refers to displacements greater than those corresponding to the maximum load. **Figure 17** shows the edges of the laminates for samples I-A-03, II-A-03, III-A-03, which were captured from the longitudinal dissection of the samples, close to the damage region, after the tests. Class A samples denoted a similar shear mode in the failure. Unfortunately, the experiments did not provide information on the damage sequence and its locations. Only the Class A samples were dissected, as they showed more accentuated failures in the laminate than the samples from the other classes.

a) I-A-03 b) II-A-01 c) III-A-03

Figure 17: Side view of the crack path of dissected samples.

Figure 18 shows cuts made in the middle section of the sample I-A-01, where the compressive displacement was interrupted when it reached 9.0 mm. **Figure 18a** shows a failure propagation from the outer surface and oriented in the circumferential direction (fiberglass direction), located in the central part close to the perforation. The photo in **Figure 18b** shows the cross-section in the perforation diameter, where a longitudinal cut (**Figure 18c**) was also performed. It is also observed delamination and crack opening through the laminate thickness.

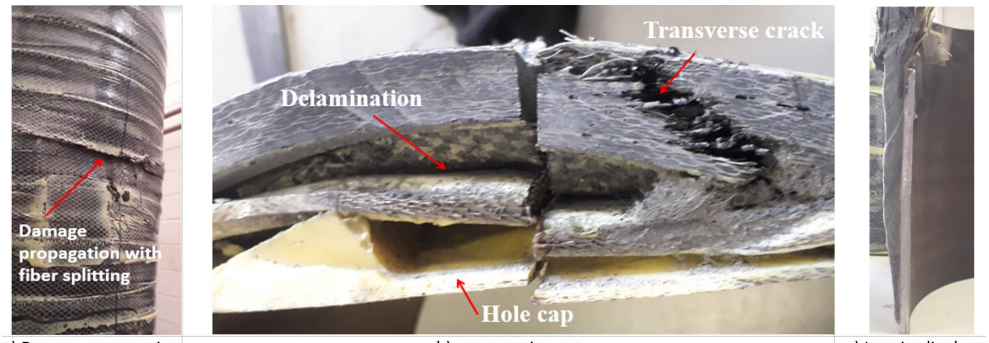

a) Damage propagation b) cross section cut c) Longitudinal cut

Figure 18: Laminate failure examples.

Figure 19a shows the repairs of the I-B-01 tube, after the axial compression test, corresponding to a final displacement of 7.47 mm, and no failure was developed on the laminate surface. **Figure 19b,c** shows the transverse and longitudinal sections cut close to the perforation, where it is observed that there were no failures in the laminate (delamination, cracking or interface defect). Also, no failure was observed in the steel tube, such as the folding of the section at the perforation's edges.

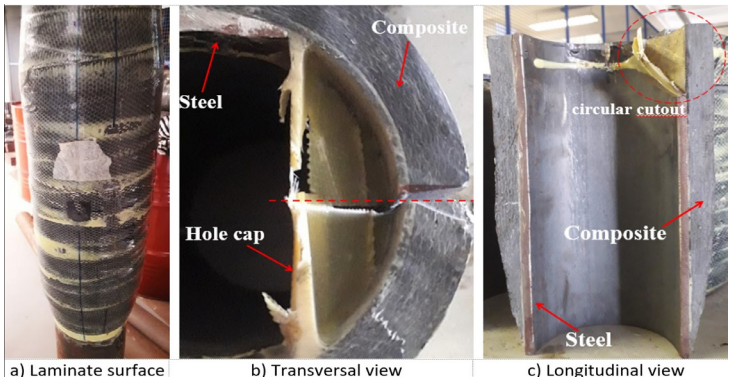

a) Laminate surface b) Transversal view c) Longitudinal view

Figure 19: Repair of the I-B-01 sample after being tested.

Figure 20a shows the repair of I-C-03 tube, corresponding to a final displacement of 5 mm. **Figure 20b** shows the final configuration of the tube, where no damage was observed on the laminate surface. **Figure 20c** shows a delamination failure located close to the perforation and in the direction of fiberglass orientation (circumferential direction). It is observed that delamination starts from the perforation edge to the circumferential direction.

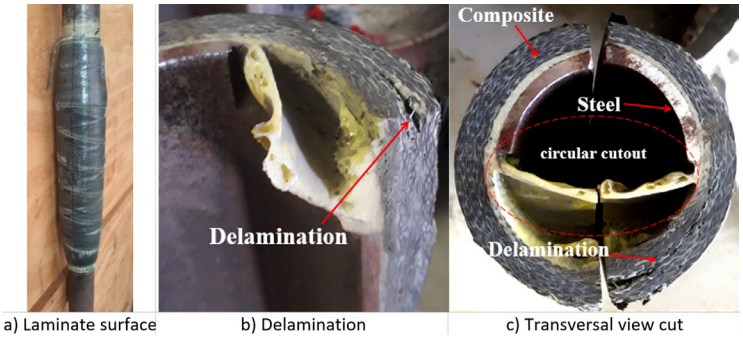

Figure 20: Repair of the I-C-03 sample after being tested.

4. CONCLUSIONS

This research analyzes the effectiveness of three distinct types of CFRP patch laminates to recover the compressive load bearing capacity of perforated tubular members from flare-boom structures. The repair patch thicknesses were established through numerical simulations, and experiments with the indicated thicknesses were performed. Numerical predictions for repair were conducted for three length-diameter ratios, a total of twenty-seven specimens were evaluated in compression, up to maximum load. For each type of material, a summary of the repair procedure was presented, describing the different methods of preparing the substrate surface, the lamination technique, and the curing process.

In an overall evaluation of the CFRP patch repair campaign of perforated tubular members, a strong correlation was observed between numerical estimations of the repair thicknesses, for each material type, required to recover the lost capacity and the capacity measured experimentally in repaired samples. This indicates both the success of the strategy for repair sizing and the effectiveness of this kind of repair. The compressive strength of all repaired samples was higher than that of unrepaired perforated tubes, especially for Class B and C tubes, where the damage represents greater cross-sectional loss. The work reported here is relevant for structural repair of offshore tubular members when compared to the experimentally observed behavior of perforated steel tubular members at full scale under axial compression. Because tubular members are frequently subjected to bending, tension, compression, or a combination of these loads in different proportions, further studies are then required to ascertain the repair effectiveness.

Acknowledgments

The authors acknowledge the support from the National Council for Scientific and Technological Development (CNPq) and National Agency of Petroleum, Natural Gas and Biofuels (ANP).

Author's Contributions: Jorge L. Martinez: Methodology, Software, Formal Analysis, Writing – original draft preparation. Julio C. R. Cyrino: Conceptualization, Methodology, Formal analysis, Supervision, Writing – review. Murilo A. Vaz: Conceptualization, Investigation, Formal analysis, Writing – review & editing, Supervision, Funding acquisition, Project administration. Irving D. Hernández: Methodology, Software, Investigation, Data Curation, Formal analysis, Validation, Writing – review, editing, creation and presentation. Victor D. Torres: Methodology, Software, Visualization. Valber A. Perrut: Conceptualization, Writing – review, Resources. Gustavo Gomes de Paula: Conceptualization, Writing – review, Resources.

Editor: Marco L. Bittencourt

References

Alexander, C., & Bedoya, J. (2011). An updated perspective on using composite materials to reinforce offshore pipelines and risers. *Proc. of IOPF*, 1–18.

Alexander, C., & Ochoa, O. O. (2010). Extending onshore pipeline repair to offshore steel risers with carbon–fiber reinforced composites. *Composite Structures, 92*(2), 499–507. https://doi.org/10.1016/j.compstruct.2009.08.034

ASTM. (2015). *D5023—Test Method for Plastics: Dynamic Mechanical Properties: In Flexure (Three-Point Bending).* ASTM International. https://doi.org/10.1520/D5023-15

ASTM. (2016). *D3528—Test Method for Strength Properties of Double Lap Shear Adhesive Joints by Tension Loading.* ASTM International. https://doi.org/10.1520/D3528-96R16

Cerik, B. C., Shin, H. K., & Cho, S.-R. (2016). A comparative study on damage assessment of tubular members subjected to mass impact. *Marine Structures, 46*, 1–29. https://doi.org/10.1016/j.marstruc.2015.11.002

Chan, P. H., Tshai, K. Y., Johnson, M., & Li, S. (2015). The flexural properties of composite repaired pipeline: Numerical simulation and experimental validation. *Composite Structures, 133*, 312–321. https://doi.org/10.1016/j.compstruct.2015.07.066

Chen, Y., Chen, X., & Wang, C. (2016). Web crippling of galvanized steel tube strengthened by CFRP sheets. *Composites Part B: Engineering, 84*, 200–210. https://doi.org/10.1016/j.compositesb.2015.08.083

Dassault Systèmes. (2009). *ABAQUS/Standard User's Manual, Version 6.13.* Dassault Systèmes.

Esmaeel, R. A., Khan, M. A., & Taheri, F. (2012). Assessment of the Environmental Effects on the Performance of FRP Repaired Steel Pipes Subjected to Internal Pressure. *Journal of Pressure Vessel Technology, 134*(4), 041702. https://doi.org/10.1115/1.4005944

George JM, Kimiaei M, Elchalakani M, Fawzia S. (2021). Experimental and numerical investigation of underwater composite repair with fibre reinforced polymers in corroded tubular offshore structural members under concentric and eccentric axial loads. Eng Struct [Internet]. 227(June 2020):111402. https://doi.org/10.1016/j.engstruct.2020.111402

Hassanein MF, Elchalakani M, Elkawas AA. (2017). Design of cold-formed CHS braces for steel roof structures. Thin-Walled Struct [Internet]. 120(August):249–259. https://doi.org/10.1016/j.tws.2017.09.002

Hernández, I. D., Vaz, M. A., Cyrino, J. C. R., & Alvarez, N. M. R. (2019). Three-dimensional image-based approach for imperfect structures surface modeling. *Journal of the Brazilian Society of Mechanical Sciences and Engineering, 41*(9). https://doi.org/10.1007/s40430-019-1873-x

Hernández, I. D., Vaz, M. A., Cyrino, J. C. R., & Liang, D. A. (2018). Compressive capacity of perforated tubular members using symbolic regression of DoE-FEM simulations. *Thin-Walled Structures, 131*, 440–450. https://doi.org/10.1016/j.tws.2018.07.033

Hollaway, L. C., & Cadei, J. (2002). Progress in the technique of upgrading metallic structures with advanced polymer composites. *Prog. Struct. Engng Mater*, 131–148. https://doi.org/10.1002/pse.112

Imran M, Mahendran M, Keerthan P. (2018). Experimental and numerical investigations of CFRP strengthened short SHS steel columns. Eng Struct [Internet]. 175(September):879–894. https://doi.org/10.1016/j.engstruct.2018.08.042

ISO. (2006). *ISO/TS 24817:2006—Petroleum, Petrochemical and Natural Gas Industries. Composite Repairs for Pipe Work—Qualification and Design, Installation, Testing and Inspection.* ISO.

Joven, R., & Minaie, B. (2018). Thermal properties of autoclave and out-of-autoclave carbon fiber-epoxy composites with different fiber weave configurations. *Journal of Composite Materials, 52*(29), 4075–4085. https://doi.org/10.1177/0021998318774608

Kabir MH, Fawzia S, Chan THT, Badawi M. (2016). Numerical studies on CFRP strengthened steel circular members under marine environment. Mater Struct Constr. 49(10):4201–4216.

Khedmati, M. R., & Nazari, M. (2012). A numerical investigation into strength and deformation characteristics of preloaded tubular members under lateral impact loads. *Marine Structures, 25*(1), 33–57. https://doi.org/10.1016/j.marstruc.2011.07.003

Lan X, Chan TM, Young B. (2017), Static strength of high strength steel CHS X-joints under axial compression. J Constr Steel Res [Internet]. 138:369–379. https://doi.org/10.1016/j.jcsr.2017.07.003

Liu J ping, Yang J, Chen B chun, Zhou Z yuan. (2020). Mechanical performance of concrete-filled square steel tube stiffened with PBL subjected to eccentric compressive loads: Experimental study and numerical simulation. Thin-Walled Struct [Internet]. 149(February):106617. https://doi.org/10.1016/j.tws.2020.106617

Mohammed, A. A., Manalo, A. C., Maranan, G. B., Muttashar, M., Zhuge, Y., Vijay, P. V., & Pettigrew, J. (2020). Effectiveness of a novel composite jacket in repairing damaged reinforced concrete structures subject to flexural loads. *Composite Structures, 233*, 111634. https://doi.org/10.1016/j.compstruct.2019.111634

Murakami, S., Nishimura, N., Takeuchi, S., Inoguchi, H., & Jikuya, K. (1998). Ultimate Strength of Cylindrical Tubular Columns with Circular Perforation. In N. Shanmugam, J. Liew, & V. Thevendran (Eds.), *Thin-Walled Structures: Research and Development—Volume 2* (1st ed., pp. 587–596). Elsevier.

Nishimura, N., Murakami, S., Takeuchi, S., & Asoda, S. (1996). Experimental Study on Buckling Strength of the Perforated Cylindrical Steel Tubular Members. *JSSC, 3*(10), 29–38. https://doi.org/10.11273/jssc1994.3.10_29

Okada, H., Masaoka, K., Katsura, S., & Matsui, T. (2004). A study on deterioration of strength and reliability of aged jacket structures. *Oceans '04 MTS/IEEE Techno-Ocean '04 (IEEE Cat. No.04CH37600), 1*, 186–192. https://doi.org/10.1109/OCEANS.2004.1402915

Siwowski, T. W., & Siwowska, P. (2018). Experimental study on CFRP-strengthened steel beams. *Composites Part B: Engineering, 149*, 12–21. https://doi.org/10.1016/j.compositesb.2018.04.060

Subhani, M., & Al-Ameri, R. (2016). Strength reduction in square columns confined with CFRP under marine environment. *Composites Part B: Engineering, 97*, 183–192. https://doi.org/10.1016/j.compositesb.2016.05.016

Tafsirojjaman T, Fawzia S, Thambiratnam D, Zhao XL. (2020). Numerical investigation of CFRP strengthened RHS members under cyclic loading. Structures [Internet]. 24(February):610–626. https://doi.org/10.1016/j.istruc.2020.01.041

Tong, L., Xu, G., Zhao, X.-L., Zhou, H., & Xu, F. (2019). Experimental and theoretical studies on reducing hot spot stress on CHS gap K-joints with CFRP strengthening. *Engineering Structures, 201*, 109827. https://doi.org/10.1016/j.engstruct.2019.109827

Vaz, M. A., Cyrino, J. C. R., Hernández, I. D., Zegarra, V. D., Martinez, J. L., & Liang, D. A. (2018). Experimental and numerical analyses of the ultimate compressive strength of perforated offshore tubular members. *Marine Structures, 58*, 1–17. https://doi.org/10.1016/j.marstruc.2017.10.010

Vijay, P. V., Soti, P. R., GangaRao, H. V. S., Lampo, R. G., & Clarkson, J. D. (2016). Repair and Strengthening of Submerged Steel Piles Using GFRP Composites. *Journal of Bridge Engineering, 21*(7), 04016038. https://doi.org/10.1061/(ASCE)BE.1943-5592.0000903

Yang, J., Wang, J., & Wang, Z. (2020a). Axial compressive behavior of partially CFRP confined seawater sea-sand concrete in circular columns – Part I: Experimental study. *Composite Structures, 246*(April), 112373. https://doi.org/10.1016/j.compstruct.2020.112373

Yang, J., Wang, J., & Wang, Z. (2020b). Axial compressive behavior of partially CFRP confined seawater sea-sand concrete in circular columns – Part II: A new analysis-oriented model. *Composite Structures, 246*(April), 112368. https://doi.org/10.1016/j.compstruct.2020.112368

Yu, Z., & Amdahl, J. (2018). A review of structural responses and design of offshore tubular structures subjected to ship impacts. *Ocean Engineering, 154*, 177–203. https://doi.org/10.1016/j.oceaneng.2018.02.009

Zeinoddini, M., Ezzati, M., & Fakheri, J. (2014). Uniaxial strain ratcheting behavior of dented steel tubular: An experimental study. *Engineering Failure Analysis, 44*, 202–216. https://doi.org/10.1016/j.engfailanal.2014.05.016

Zhao Y, Zhai X, Wang J. 2019. Buckling behaviors and ultimate strengths of 6082-T6 aluminum alloy columns under eccentric compression – Part I: Experiments and finite element modeling. Thin-Walled Structures 143(2):106207.